Supporting Information

Fluorescent Molybdenum Oxide Quantum Dots and Hg^{II} Synergistically Accelerate the Cobaltporphyrin Formation: a New Strategy for Trace Hg^{II} Analysis

Li Zhang,[a] Zhao-Wu Wang,[b] Sai-Jin Xiao,[c] Dong Peng,[a] Jia-Qing Chen,[a] Ru-Ping Liang,[a] Jun Jiang[b,*] and Jian-Ding Qiu[a,*]

[a]*College of Chemistry, Nanchang University, Nanchang, 330031, China. Fax: (+86) 791-83969518, E-mail: jdqiu@ncu.edu.cn*

[b]*Hefei National Laboratory for Physical Sciences at the Microscale, Collaborative Innovation Center of Chemistry for Energy Materials, School of Chemistry and Materials Science, University of Science and Technology of China, Hefei 230026, China. E-mail: jiangj1@ustc.edu.cn.*

[c]*School of Chemistry, Biology and Material Science, East China University of Technology (ECUT), Nanchang 330013, China.*

Preparation of MoO_{3-x} QDs: According to our recently reported method,[1] the MoO_{3-x} QDs were prepared by using commercial MoS_2 powder as the precursor and H_2O_2 as the oxidant. In brief, 900.0 mg of MoS_2 powder was mixed with 72.0 mL of 30% H_2O_2 and 18.0 mL of H_2O, and stirred at room temperature for 120 min, then the pH was adjusted to 7.0 with 3.375 mL of 425 mg/mL of sodium hydroxide (NaOH), followed by stirring for another 120 min. Finally, MoO_{3-x} QDs were obtained by centrifugation at 12000 rpm for 5 min to remove large particles and then dialysis for 62 h to remove the byproducts with a 500-1000 Da MWCO dialysis tube.

Characterization of MoO_{3-x} QDs

Raman spectroscopy and FTIR measurements were carried out to confirm the phase evolution from MoS_2 to molybdenum oxide QDs. The Raman spectra of MoS_2 precursors and the molybdenum oxide products are shown in Figure S1a. The peak positions of the molybdenum oxide QDs are completely different from those of bulk MoS_2 powders with normal Raman peaks at about 378 and 403 cm^{-1} corresponding to the E^1_{2g} and the A_{1g} active modes of MoS_2 (Figure S1a inset), respectively. Specifically, the peak at 998 cm^{-1} is assigned to the terminal oxygen (Mo＝O) stretching vibrations of MoO_3. The peaks at 898 and 845 cm^{-1} are due to the stretching vibrations of doubly coordinated bridging oxygen (Mo_2-O). The bands at 630 and 470 cm^{-1} are due to the stretching mode of triply coordinated oxygen (Mo_3-O) (Figure S1a).[2-3] In the FTIR spectrum of molybdenum oxide QDs, the peak at 990 cm^{-1} can be attributed to the stretching vibration of Mo＝O, indicating the layered orthorhombic MoO_3 phase. The strong absorption at 825 cm^{-1} is due to the doubly coordinated oxygen (Mo_2-O) stretching mode of the Mo^{6+} ions. The bands at 620 and 493 cm^{-1} are assigned to the characteristics of the Mo_3-O units (Figure S1b). The spectroscopic characterizations indicate the main phase of the molybdenum oxide QDs as orthorhombic MoO_3. The XRD pattern of the molybdenum oxide (Figure S1c) shows that the molybdenum oxide QDs are of high crystallinity with relatively sharp and strong peaks. The (020) peak at 2θ of 12.8° appears clearly, indicating the presence of the orthorhombic phase.[1,4] However, the XRD pattern of molybdenum oxide QDs does not perfectly match with the orthorhombic MoO_3 (JCPDS card No. 35-0609), which is probably due to the formation of some oxygen-deficient byproduct in the preparation procedures.[5] Namely, partial Mo^{IV} in MoS_2 precursors is oxidized to Mo^{V} by H_2O_2, forming the slightly oxygen-deficient molybdenum oxide nanostructures. The presence of subvalent Mo^{V} could also be reflected by the appearance of a brownish color (Figure 1d inset), uncharacteristic for pure MoO_3.[6]

The molybdenum oxide QDs were analyzed by XPS in order to identify the valence state of Mo and

S. Compared with the high-resolution XPS spectra of MoS_2 precursors (Figure S2), the S 2p doublets of the obtained molybdenum oxide QDs shift to the higher binding energy pair. The S $2p_{3/2}$ and S $2p_{1/2}$ components at 168.8 and 170.0 eV can be identified as the S 2p peaks of oxidized sulphur (SO_4^{2-}) which would disappear after dialysis for 48 h in water (Figure S3b and Figure S4). The corresponding XPS spectra in the O ls energy region are shown in Figure S3c where peaks associated with oxides and chemisorbed oxygen can be distinguished. The peaks near 530.0 eV are assigned to lattice oxygen atoms of MoO_{3-x}, while the peaks at higher binding energies near 531.8 eV are identified as those from chemisorbed oxygen atoms on surface of MoO_{3-x}.[7-9]

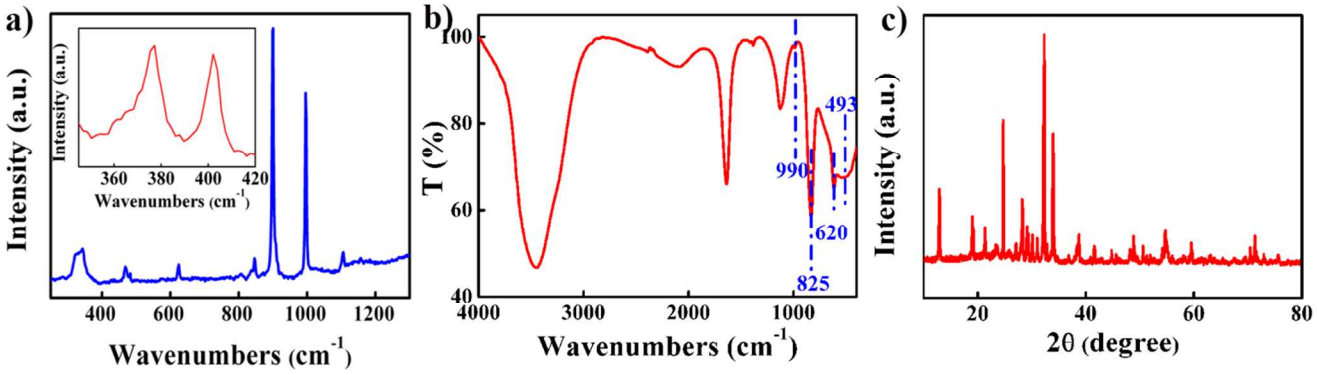

Figure S1. (a) Raman spectrum of MoO_{3-x} QDs; inset: Raman spectrum of MoS_2 powder. (b) FTIR spectrum and (c) XRD pattern of MoO_{3-x} QDs.

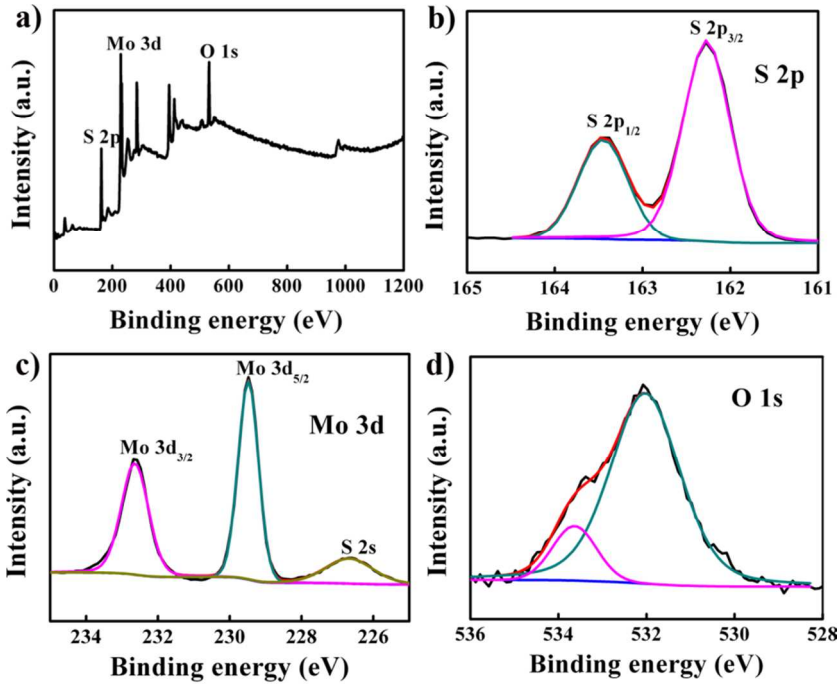

Figure S2. (a) Survey XPS pattern of MoS_2 powders. (b) High-resolution S 2p, (c) Mo 3d, and (d) O 1s spectra of MoS_2 powders.

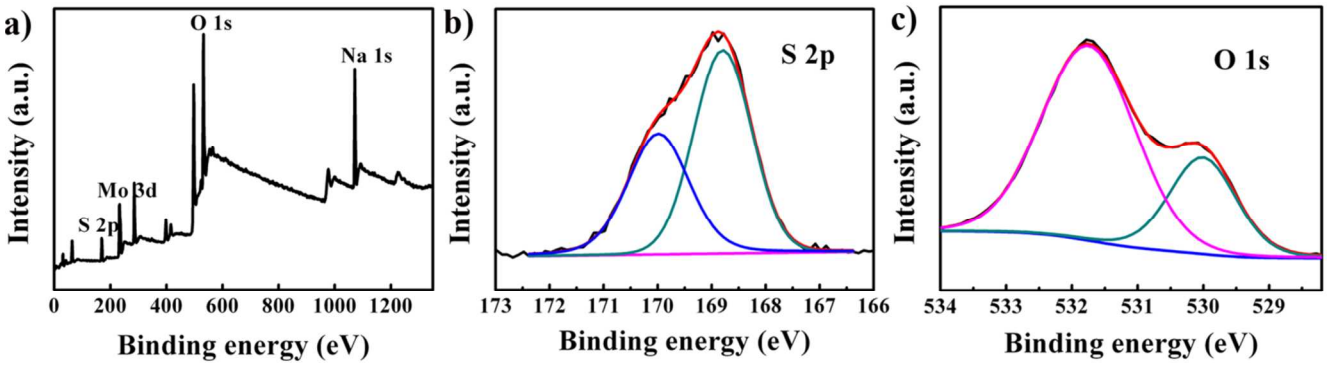

Figure S3. (a) Survey XPS pattern of MoO_{3-x} QDs. High-resolution S 2p (b) and O 1s (c) spectra of MoO_{3-x} QDs.

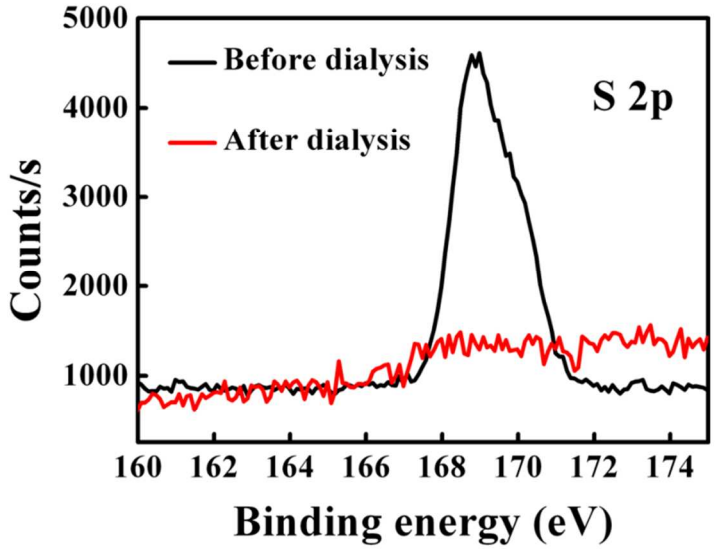

Figure S4. High-resolution XPS spectra of S 2p before and after dialysis for 48 h in water.

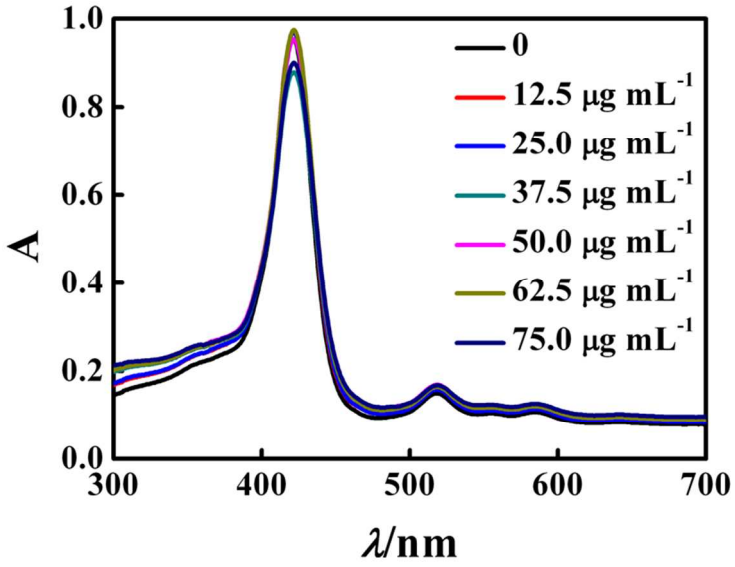

Figure S5. UV-vis absorption spectra of 12.5 μM TMPyP in the presence of different concentrations of MoO_{3-x} QDs.

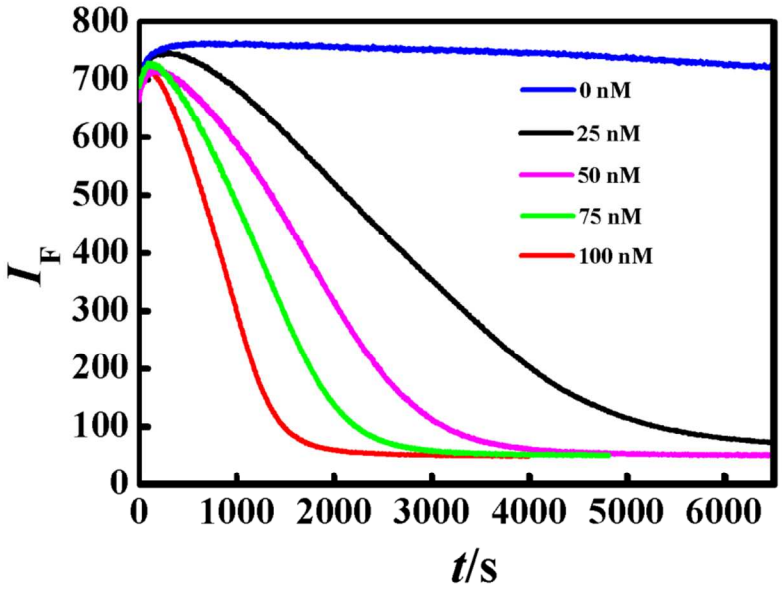

Figure S6. Fluorescence intensity of 12.5 μM TMPyP at 658 nm with excitation at 420 nm *versus* reaction time in the presence of 50 μM Co^{II}, 50 μg mL^{-1} MoO_{3-x} QDs, and different concentrations of Hg^{II}.

Table S1. The computed bonding energy (E_b) for metal atoms (Ag, Al, Ca, Cd, Co, Cr, Cu, Fe, Hg, K, Mg, Mn, Ni, Pb, Sn and Zn) adsorbed to porphyrin.

Metal on porphyrin	Ag	Al	Ca	Cd	Co	Cr	Cu	Fe	Hg	K	Mg	Mn	Ni	Pb	Sn	Zn
E_b (eV)	0.51	2.05	3.12	0.04	5.07	8.23	1.97	5.79	0.15	1.88	2.01	7.25	3.67	2.33	2.59	0.04

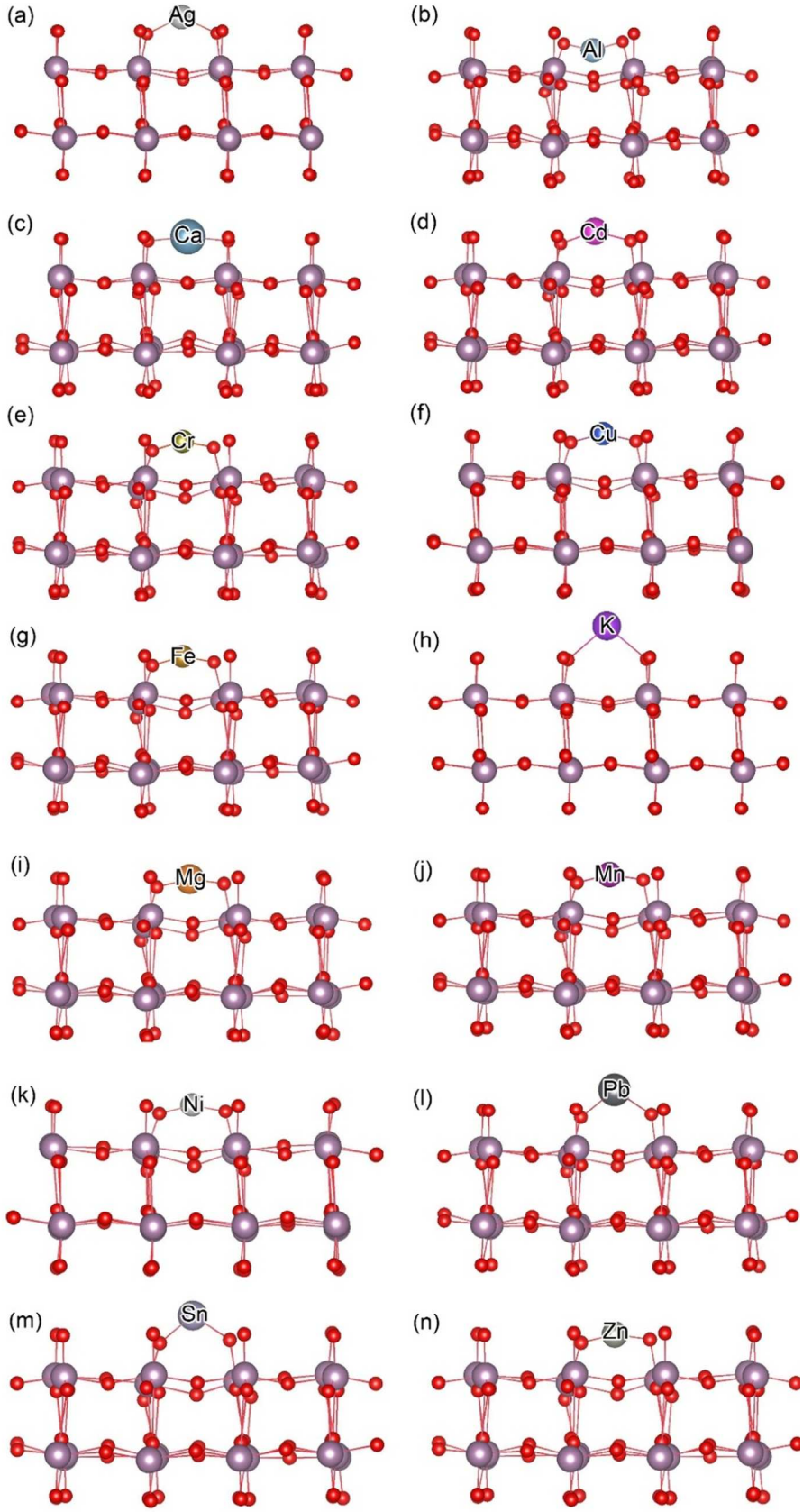

Figure S7. The simulated adsorption structures of metal atoms (Ag, Al, Ca, Cd, Cr, Cu, Fe, K, Mg, Mn, Ni, Pb, Sn and Zn for (a) to (n), respectively) on MoO_{3-x}, with bonding energies listed in Table S2.

Table S2. The computed bonding energy (E_b) for metal atoms (Ag, Al, Ca, Cd, Cr, Cu, Fe, K, Mg, Mn, Ni, Pb, Sn and Zn) adsorbed to MoO_{3-x} (Figure S7).

Metal on MoO_{3-x}	Ag	Al	Ca	Cd	Cr	Cu	Fe	K	Mg	Mn	Ni	Pb	Sn	Zn
E_b (eV)	2.72	7.38	6.15	5.71	11.04	3.65	8.69	4.74	5.52	11.64	5.15	5.71	5.72	2.45

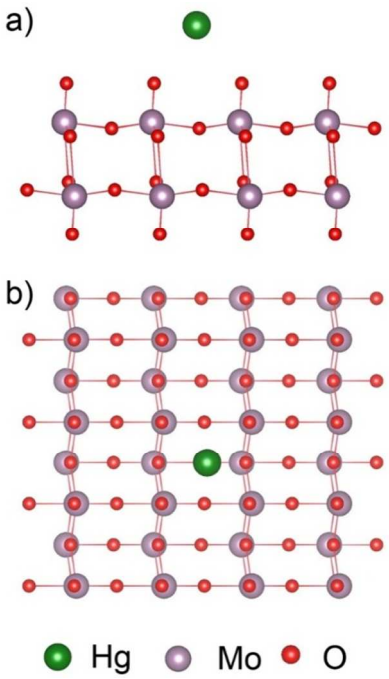

Figure S8. The side (a) and top (b) view of the simulated adsorption structure of Hg on MoO_{3-x}. The bonding energy (E_b) is 0.18 eV and the shortest Hg-O distance is 3.6 Å, indicating very weak adsorption.

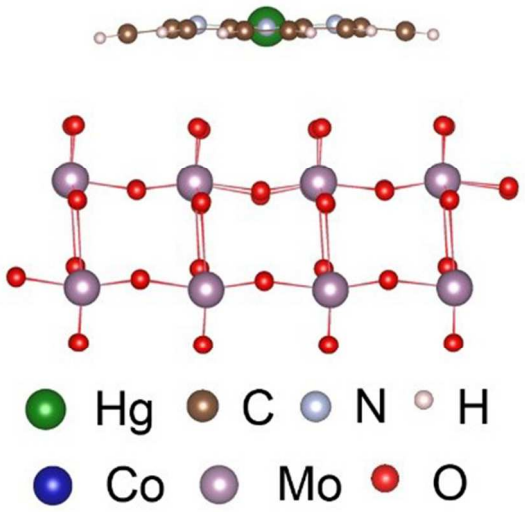

Figure S9. The simulated adsorption structure of Hg^{II}-porphyrin on MoO_{3-x} (bonding energy (E_b) is 1.80 eV).

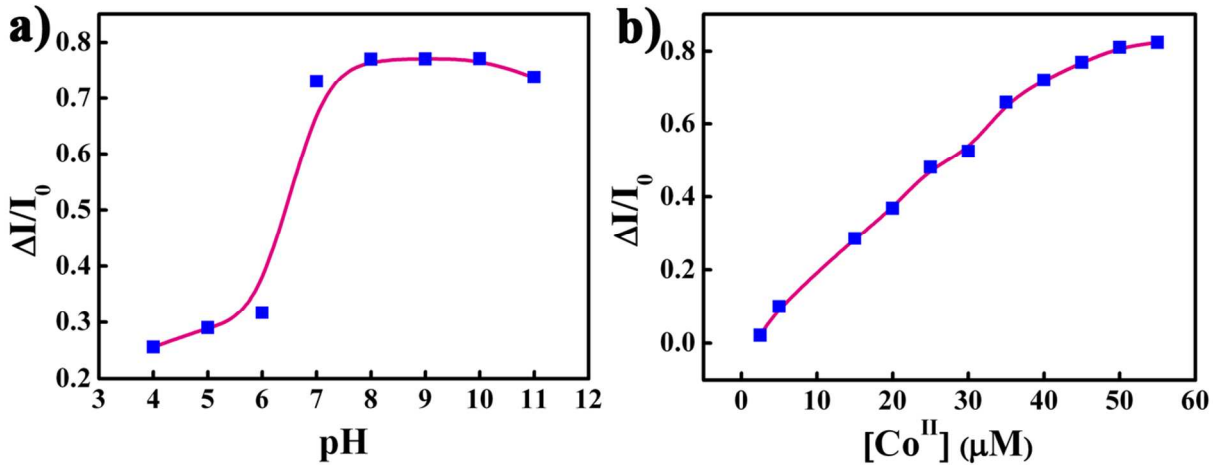

Figure S10. (a) Effects of pH values on the fluorescence quenching as a result of Co^{II}(TMPyP) formation accelerated by MoO_{3-x} QDs and Hg^{II}; the concentrations of TMPyP, Co^{II}, Hg^{II}, and MoO_{3-x} QDs were 12.5 μM, 50 μM, 100 nM, and 50 μg mL^{-1}, respectively. (b) Effects of Co^{II} concentrations on the fluorescence quenching as a result of Co^{II}(TMPyP) formation accelerated by MoO_{3-x} QDs and Hg^{II}; the concentrations of TMPyP, Hg^{II}, and MoO_{3-x} QDs were 12.5 μM, 100 nM, and 50 μg mL^{-1}, respectively. PB buffer, pH 7.0, 2 mM.

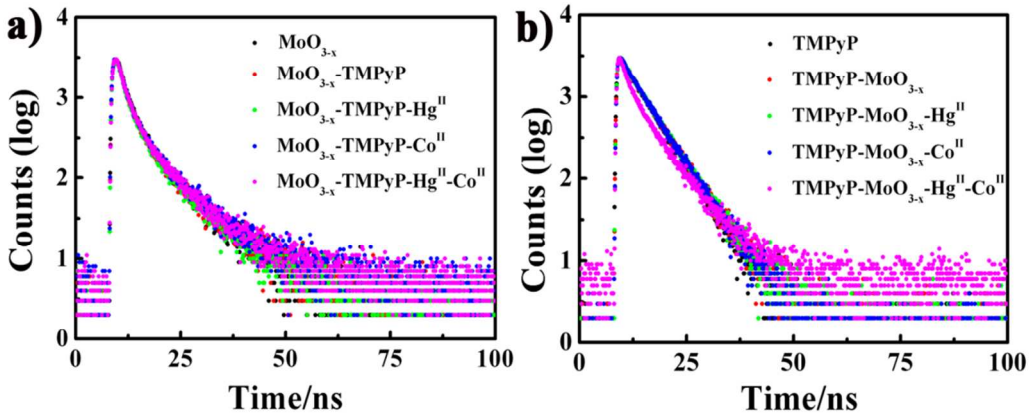

Figure S11. (a) Fluorescence decay of MoO_{3-x} QDs at 430 nm in the presence of TMPyP and/or different metal ions. (b) Fluorescence decay of TMPyP at 658 nm in the presence of MoO_{3-x} QDs and/or different metal ions. The concentrations of TMPyP, Co^{II}, Hg^{II}, and MoO_{3-x} QDs were 12.5 μM, 50 μM, 100 nM, and 50 μg mL^{-1}, respectively.

Table S3. PL lifetimes of MoO_{3-x} QDs in the presence of TMPyP and/or different metal ions.

Lifetime/ns	τ_1	A_1	τ_2	A_2
MoO_{3-x}	2.08	83%	7.95	17%
MoO_{3-x}-TMPyP	2.03	85%	8.03	15%
MoO_{3-x}-TMPyP-Hg^{II}	1.99	85%	7.88	15%
MoO_{3-x}-TMPyP-Co^{II}	1.99	83%	8.06	17%
MoO_{3-x}-TMPyP-Co^{II}-Hg^{II}	2.01	83%	7.88	17%

Table S4. PL lifetimes of TMPyP in the presence of MoO_{3-x} QDs and/or different metal ions.

Lifetime/ns	τ_1	A_1	τ_2	A_2
TMPyP	5.03	100%		
TMPyP-MoO_{3-x}	5.17	100%		
TMPyP-MoO_{3-x}-Hg^{II}	5.16	100%		
TMPyP-MoO_{3-x}-Co^{II}	5.14	100%		
TMPyP-MoO_{3-x}-Co^{II} -Hg^{II}	5.96	46%	1.84	54%

IFE corrections

On the basis of the cuvette geometry (Figure S12a) and the absorption characteristics of the aqueous solution of TMPyP and MoO_{3-x} QDs, the IFE was corrected with the following equation.[10-11]

$$CF = \frac{F_{cor}}{F_{obsd}} = \frac{2.3dA_{ex}}{1-10^{-dA_{ex}}} 10^{gA_{em}} \frac{2.3sA_{em}}{1-10^{-sA_{em}}}$$

Where, CF is the corrected factor; F_{obsd} is the observed fluorescence intensity of MoO_{3-x} QDs and F_{cor} is the corrected fluorescence intensity by removing IFE from F_{obsd}; A_{ex} and A_{em} represent the absorbances per centimeter at the excitation wavelength and the emission wavelength of MoO_{3-x} QDs, respectively; s is the thickness of excitation beam (0.10 cm), g is the distance between the edge of the excitation beam and the edge of the cuvette (0.40 cm) and d is the width of the cuvette (1.00 cm). The maximum value of the correction factor could not exceed 3; otherwise the correction was not convincing.

Table S5 summarizes the concentrations of TMPyP, absorbance and fluorescence intensity of MoO_{3-x} QDs after each addition of TMPyP. The correction factor (CF) of IFE at each concentration of TMPyP was calculated. Figure S12b demonstrates the quenching efficiency of totally observed (E_{obsd}, black curve) and corrected (E_{cor}, red curve, after removing IFE) fluorescence of MoO_{3-x} QDs. We found that the majority of the quenching effect came from the IFE of TMPyP. After removing the IFE, the small remaining quenching effect may come from the weak electrostatic interaction between TMPyP and MoO_{3-x} QDs.[12-13]

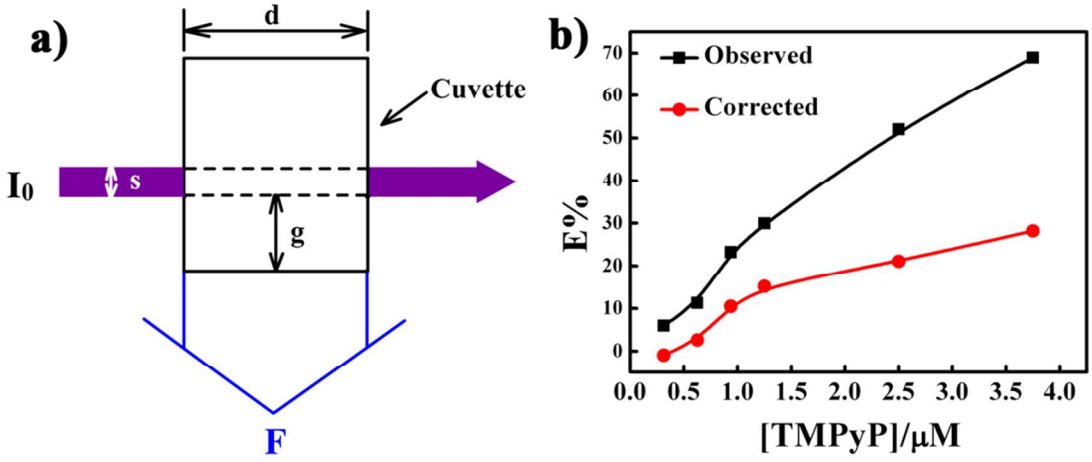

Figure S12. (a) Parameters used in the equation to correct for the inner filter effect. I_0 represents the excitation beam, F represents the observed fluorescence beam. (b) Observed (black curve, E_{obsd}) and corrected (red curve, E_{cor}) quenching efficiency of TMPyP towards MoO_{3-x} QDs. E = 1 - F/F_0, F_0 and F are the fluorescence intensities of MoO_{3-x} QDs in the absence and presence of TMPyP, respectively.

Table S5. IFE of TMPyP on the fluorescence of MoO_{3-x} QDs.

TMPyP (μM)	A_{ex}[a]	A_{em}[b]	CF[c]	F_{obsd}[d]	F_{cor}[e]	$F_{cor,0}/F_{cor}$[f]	E_{obsd}[g]	E_{cor}[h]
0.0	0.081	0.017	1.11	2739	3048.9	1	0	0
1.25	0.098	0.067	1.20	2576	3077.5	0.991	6%	-1%
2.5	0.093	0.094	1.22	2430	2968.9	1.027	11%	3%
3.75	0.098	0.147	1.30	2103	2729.4	1.117	23%	10%
5	0.095	0.187	1.35	1918	2586.0	1.179	30%	15%
6.25	0.119	0.457	1.83	1314	2405.5	1.267	52%	21%
7.5	0.134	0.771	2.58	850	2189.0	1.393	69%	28%

[a]A_{ex} is the absorbance of MoO_{3-x} QDs with the addition of TMPyP at the excitation wavelength. [b]A_{em} is the absorbance of MoO_{3-x} QDs with the addition of TMPyP at the emission wavelength. [c]Corrected factor (CF) was calculated as F_{cor}/F_{obsd}. [d]F_{obsd} is the measured fluorescence intensity of MoO_{3-x} QDs with the addition of TMPyP. [e]F_{cor} is the corrected fluorescence intensity by removing IFE from the measured fluorescence intensity. [f]$F_{cor,0}$ and F_{cor} are the corrected fluorescence intensities of MoO_{3-x} QDs in the absence and presence of TMPyP, respectively. [g]$E_{obsd} = 1 - F_{obsd}/F_{obsd,0}$, $F_{obsd,0}$ and F_{obsd} are the observed fluorescence intensities of MoO_{3-x} QDs in the absence and presence of TMPyP, respectively. [h]$E_{cor} = 1 - F_{cor}/F_{cor,0}$, $F_{cor,0}$ and F_{cor} are the corrected fluorescence intensities of MoO_{3-x} QDs in the absence and presence of TMPyP, respectively.

Table S6. Comparison of the performance of different methods for Hg^{II} sensing and imaging.

Detection methods	Materials	Linear range (nM)	Detection limit (nM)	Imaging target	Ref.
Fluorescent	Rhodamine B selenolactone	100-5000	23	cells	[14]
Colorimetric, Fluorescent	3D Au@MoS_2 heterostructure, rhodamine B	5000-50000	0.038 0.22	Cells and mice	[15]
Fluorescent	Organic fluorophores (1-CN)	0-10000	800	cells	[16]
Bioluminescent	Caged luciferin	2500-15000	-	mice	[17]
Fluorescent	RBITC-PEG-AuNPs	10-500	2.3	cells	[18]
Fluorescent	Rhodamine-BODIPY	0-40000	14.1	cells	[19]
Fluorescent	ICT molecules	0-290	10	cells	[20]
Fluorescent	Rhodamine/BODIPY	0-300	8	cells	[21]
Fluorescent	phenothiazine-based probes	20-330	15	cells	[22]
Fluorescent	N, S-doped carbon dots	0-300	1.37	E. coli	[23]
Fluorescent	NAC-QDs, Rhodamine 6G	24.9-1246.3	3.7	cells	[24]
Fluorescent	Carbon nanoparticles	1000-18000	100	cells	[25]
Colorimetric, Fluorescent	TMPyP, MoO_{3-x} QDs, Co^{II}	5-87.5 5-100	0.6 0.8	cells	This work

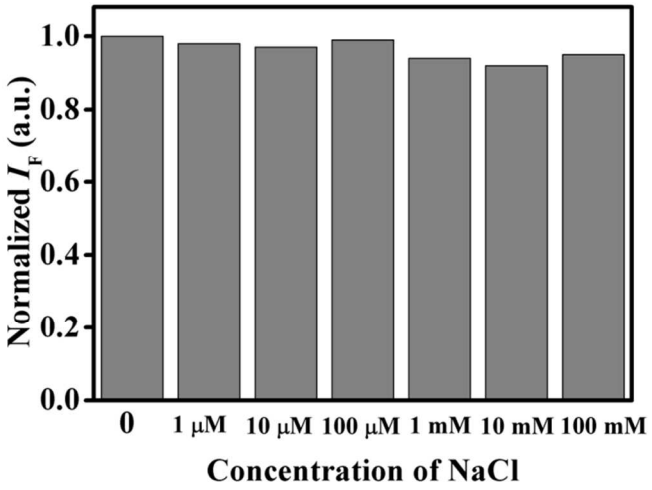

Figure S13. Fluorescence variation of MoO_{3-x} QDs at different concentrations of NaCl.

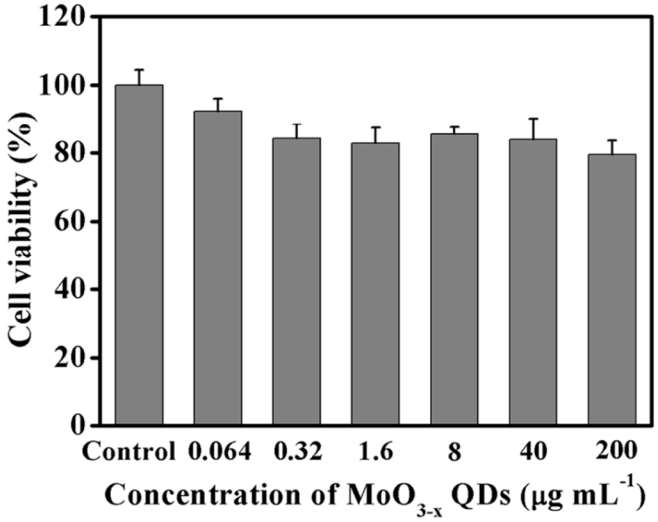

Figure S14. Effect of MoO_{3-x} QDs on A549 cells viability.

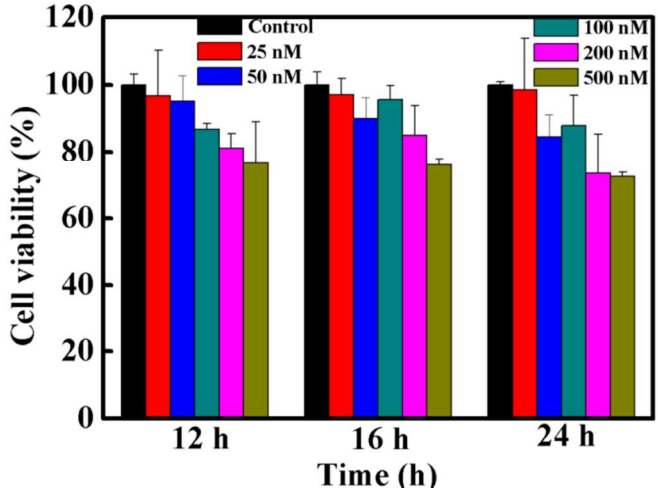

Figure S15. Cell viability of A549 cells after 12 to 24 hours of incubation with various concentrations of Hg^{II}.

Table S7. Analytical results for the determination of Hg^{II} in river water samples using the proposed method and the ICP-MS method.

Sample	Added (nM)	The present method		ICP-MS method	
		Found (mean ± SD, n=3, nM)	Recovery (%)	Found (mean ± SD, n=3, nM)	Recovery (%)
River water	0	-	-	-	-
	20	20.84 ± 0.05	104.2	20.18 ± 0.02	100.9
	50	51.35 ± 0.07	102.7	51.24 ± 0.01	102.5
	80	81.53 ± 0.03	101.9	81.36 ± 0.03	101.7

References:

(1) Xiao, S. J.; Zhao, X. J.; Hu, P. P.; Chu, Z. J.; Huang, C. Z.; Zhang, L. Highly Photoluminescent Molybdenum Oxide Quantum Dots: One-Pot Synthesis and Application in 2,4,6-Trinitrotoluene Determination. *ACS Appl. Mater. Interfaces* **2016**, *8*, 8184-8191.

(2) Song, G.; Shen, J.; Jiang, F.; Hu, R.; Li, W.; An, L.; Zou, R.; Chen, Z.; Qin, Z.; Hu, J. Hydrophilic Molybdenum Oxide Nanomaterials with Controlled Morphology and Strong Plasmonic Absorption for Photothermal Ablation of Cancer Cells. *ACS Appl. Mater. Interfaces* **2014**, *6*, 3915-3922.

(3) Seguin, L.; Figlarz, M.; Cavagnat, R.; Lassègues, J. C. Infrared and Raman Spectra of MoO_3 Molybdenum Trioxides and $MoO_3 \cdot xH_2O$ Molybdenum Trioxide Hydrates. *Spectrochim. Acta A* **1995**, *51*, 1323-1344.

(4) Klinbumrung, A.; Thongtem, T.; Thongtem, S. Characterization of Orthorhombic α-MoO_3 Microplates Produced by a Microwave Plasma Process. *J. Nanomater.* **2012**, *2012*, 1-5.

(5) Krishnan, C. V.; Chen, J.; Burger, C.; Chu, B. Polymer-Assisted Growth of Molybdenum Oxide Whiskers via a Sonochemical Process. *J. Phys. Chem. B* **2006**, *110*, 20182-20188.

(6) Muñoz-Espí, R.; Burger, C.; Krishnan, C. V.; Chu, B. Polymer-Controlled Crystallization of Molybdenum Oxides from Peroxomolybdates: Structural Diversity and Application to Catalytic Epoxidation. *Chem. Mater.* **2008**, *20*, 7301-7311.

(7) Ma, F.; Yuan, A.; Xu, J.; Hu, P. Porous α-MoO_3/MWCNT Nanocomposite Synthesized via a Surfactant-Assisted Solvothermal Route as a Lithium-Ion-Battery High-Capacity Anode Material with Excellent Rate Capability and Cyclability. *ACS Appl. Mater. Interfaces* **2015**, *7*, 15531-15541.

(8) Yang, S.; Wang, Z.; Hu, Y.; Luo, X.; Lei, J.; Zhou, D.; Fei, L.; Wang, Y.; Gu, H. Highly Responsive Room-Temperature Hydrogen Sensing of α-MoO_3 Nanoribbon Membranes. *ACS Appl. Mater. Interfaces* **2015**, *7*, 9247-9253.

(9) Diskus, M.; Nilsen, O.; Fjellvag, H. Growth of Thin Films of Molybdenum Oxide by Atomic Layer Deposition. *J. Mater. Chem.* **2011**, *21*, 705-710.

(10) Gauthier, T. D.; Shane, E. C.; Guerin, W. F.; Seitz, W. R.; Grant, C. L. Fluorescence Quenching Method for Determining Equilibrium Constants for Polycyclic Aromatic Hydrocarbons Binding to Dissolved Humic Materials. *Environ. Sci. Technol.* **1986**, *20*, 1162-1166.

(11) Zhai, W.; Wang, C.; Yu, P.; Wang, Y.; Mao, L. Single-Layer MnO_2 Nanosheets Suppressed Fluorescence of 7-Hydroxycoumarin: Mechanistic Study and Application for Sensitive Sensing of Ascorbic Acid in vivo. *Anal. Chem.* **2014**, *86*, 12206-12213.

(12) Rong, M.; Lin, L.; Song, X.; Zhao, T.; Zhong, Y.; Yan, J.; Wang, Y.; Chen, X. A Label-Free Fluorescence Sensing Approach for Selective and Sensitive Detection of 2,4,6-Trinitrophenol (TNP) in Aqueous Solution Using Graphitic Carbon Nitride Nanosheets. *Anal. Chem.* **2015**, *87*, 1288-1296.

(13) Zhang, L.; Peng, D.; Liang, R.-P.; Qiu, J.-D. Nitrogen-Doped Graphene Quantum Dots as a New Catalyst Accelerating the Coordination Reaction between Cadmium(II) and 5,10,15,20-Tetrakis(1-methyl-4-pyridinio)porphyrin for Cadmium(II) Sensing. *Anal. Chem.* **2015**, *87*, 10894-10901.

(14) Shi, W.; Sun, S.; Li, X.; Ma, H. Imaging Different Interactions of Mercury and Silver with Live Cells by a Designed Fluorescence Probe Rhodamine B Selenolactone. *Inorg. Chem.* **2010**, *49*, 1206-1210.

(15) Zhi, L.; Zeng, X.; Wang, H.; Hai, J.; Yang, X.; Wang, B.; Zhu, Y. Photocatalysis-Based Nanoprobes Using Noble Metal-Semiconductor Heterostructure for Visible Light-Driven in Vivo Detection of Mercury. *Anal. Chem.* **2017**, *89*, 7649-7658.

(16) Ding, J.; Li, H.; Wang, C.; Yang, J.; Xie, Y.; Peng, Q.; Li, Q.; Li, Z. "Turn-On" Fluorescent Probe for Mercury(II): High Selectivity and Sensitivity and New Design Approach by the Adjustment of the π-Bridge. *ACS Appl. Mater. Interfaces* **2015**, *7*, 11369-11376.

(17) Jiang, T.; Ke, B.; Chen, H.; Wang, W.; Du, L.; Yang, K.; Li, M. Bioluminescent Probe for Detecting Mercury(II) in Living Mice. *Anal. Chem.* **2016**, *88*, 7462-7465.

(18) Liu, D.; Wang, S.; Swierczewska, M.; Huang, X.; Bhirde, A. A.; Sun, J.; Wang, Z.; Yang, M.; Jiang, X.; Chen, X. Highly Robust, Recyclable Displacement Assay for Mercuric Ions in Aqueous Solutions and Living Cells. *ACS Nano*, **2012**, *6*, 10999-11008.

(19) Shen, B.; Qian, Y.; Qi, Z.; Lu, C.; Cui, Y. Near-Infrared Two-Photon Fluorescent Chemodosimeter Based on Rhodamine-BODIPY for Mercury Ion Fluorescence Imaging in Living Cells. *ChemistrySelect* **2017**, *2*, 9970-9976.

(20) Cheng, X.; Li, S.; Jia, H.; Zhong, A.; Zhong, C.; Feng, J.; Qin, J.; Li, Z. Fluorescent and Colorimetric Probes for Mercury(II): Tunable Structures of Electron Donor and p-Conjugated Bridge. *Chem. Eur. J.* **2012**, *18*, 1691-1699.

(21) Karakuş, E.; Üçüncü, M.; Emrullahoğlu, M. A Rhodamine/BODIPY-Based Fluorescent Probe for the Differential Detection of Hg(II) and Au(III). *Chem. Commun.* **2014**, *50*, 1119-1121.

(22) Vengaian, K. M.; Britto, C. D.; Sivaraman, G.; Sekar, K.; Singaravadivel, S. Phenothiazine Based Sensor for Naked-Eye Detection and Bioimaging of Hg(II) and F^- Ions. *RSC Adv.* **2015**, *5*, 94903-94908.

(23) Fu, Z.; Yao, M.; Niu, X.; Cui, F. Facile Synthesis of Highly Luminescent Co-Doped Carbon Nanodots for Rapid, Sensitive, and Label-Free Detection of Hg^{2+}. *Sens. Actuators B: Chem*. **2016**, *226*, 486-494.

(24) Hu, B.; Hu, L.-L.; Chen, M.-L.; Wang, J.-H. A FRET Ratiometric Fluorescence Sensing System for Mercury Detection and Intracellular Colorimetric Imaging in Live Hela Cells. *Biosens. Bioelectron.* **2013**, *49*, 499-505.

(25) Sharma, V.; Saini, A. K.; Mobin, S. M. Multicolour Fluorescent Carbon Nanoparticle Probes for Live Cell Imaging and Dual Palladium and Mercury Sensors. *J. Mater. Chem. B* **2016**, *4*, 2466-2476.